Time- and Spectral-resolved two-photon imaging of healthy bladder mucosa and carcinoma in situ

Riccardo Cicchi,[1] Alfonso Crisci,[2] Alessandro Cosci,[1] Gabriella Nesi,[3] Dimitrios Kapsokalyvas,[1] Saverio Giancane,[3] Marco Carini,[3] and Francesco S. Pavone [1,*]

[1]*LENS, European Laboratory for Non-Linear Spectroscopy, Via Nello Carrara 1, Sesto Fiorentino, I-50019, Italy*
[2]*University of Florence Medical School, Department of Surgical and Medical Critical Area, University of Florence, Florence, I-50100, Italy*
[3]*Division of Urology, Department of Surgical and Medical Critical Area, University of Florence, Florence, I-50100, Italy*
**rcicchi@lens.unifi.it*

Abstract: Combined non-linear imaging techniques were used to deeply image human *ex-vivo* fresh biopsies of bladder as well as to discriminate between healthy bladder mucosa and carcinoma in situ. Morphological examination by two-photon excited fluorescence and second-harmonic generation has shown a good agreement with corresponding common routine histology performed on the same samples. Tumor cells appeared slightly different in shape and with a smaller cellular-to-nuclear dimension ratio with respect to corresponding normal cells. Further differences between the two tissue types were found in both spectral emission and fluorescence lifetime distribution by performing temporal- and spectral-resolved analysis of fluorescence. This method may represent a promising tool to be used in a multi-photon endoscope, in a confocal endoscope or in a spectroscopic probe for *in-vivo* optical diagnosis of bladder cancer.

OCIS codes: (180.4315) Nonlinear microscopy; (170.3880) Medical and biomedical imaging.

References and links

1. ACS, (2006), http://www.cancer.org/downloads/STT/CAFF2006PWSecured.pdf, Cancer Facts & Figs. (2006).
2. J. C. Kah, W. K. Lau, P. H. Tan, C. J. Sheppard, and M. Olivo, "Endoscopic image analysis of photosensitizer fluorescence as a promising noninvasive approach for pathological grading of bladder cancer in situ," J. Biomed. Opt. **13**(5), 054022 (2008).
3. E. L. Larsen, L. L. Randeberg, O. A. Gederaas, C. J. Arum, A. Hjelde, C. M. Zhao, D. Chen, H. E. Krokan, and L. O. Svaasand, "Monitoring of hexyl 5-aminolevulinate-induced photodynamic therapy in rat bladder cancer by optical spectroscopy," J. Biomed. Opt. **13**(4), 044031 (2008).
4. S. Berrahmoune, N. Fotinos, L. Bezdetnaya, N. Lange, J. C. Guedenet, F. Guillemin, and M. A. D'Hallewin, "Analysis of differential PDT effect in rat bladder tumor models according to concentrations of intravesical hexyl-aminolevulinate," Photochem. Photobiol. Sci. **7**(9), 1018–1024 (2008).
5. D. Jocham, F. Witjes, S. Wagner, B. Zeylemaker, J. van Moorselaar, M. O. Grimm, R. Muschter, G. Popken, F. König, R. Knüchel, and K. H. Kurth, "Improved detection and treatment of bladder cancer using hexaminolevulinate imaging: a prospective, phase III multicenter study," J. Urol. **174**(3), 862–866, discussion 866 (2005).
6. N. Ramanujam, "Fluorescence spectroscopy of neoplastic and non-neoplastic tissues," Neoplasia **2**(1/2), 89–117 (2000).
7. M. Anidjar, O. Cussenot, S. Avrillier, D. Ettori, P. Teillac, and A. Le Duc, "The role of laser-induced autofluorescence spectroscopy in bladder tumor detection. Dependence on the excitation wavelength," Ann. N. Y. Acad. Sci. **838**(1 ADVANCES IN O), 130–141 (1998).
8. F. Koenig, F. J. McGovern, A. F. Althausen, T. F. Deutsch, and K. T. Schomacker, "Laser induced autofluorescence diagnosis of bladder cancer," J. Urol. **156**(5), 1597–1601 (1996).
9. D. Zaak, H. Stepp, R. Baumgartner, P. Schneede, R. Waidelich, D. Frimberger, A. Hartmann, R. Künchel, A. Hofstetter, and A. Hohla, "Ultraviolet-excited (308 nm) autofluorescence for bladder cancer detection," Urology **60**(6), 1029–1033 (2002).
10. W. W. Chin, P. S. P. Thong, R. Bhuvaneswari, K. C. Soo, P. W. S. Heng, and M. Olivo, "In-vivo optical detection of cancer using chlorin e6-polyvinylpyrrolidone induced fluorescence imaging and spectroscopy," BMC Med. Imaging **9**(1), 1–8 (2009).

#119986 - $15.00 USD Received 18 Nov 2009; revised 26 Jan 2010; accepted 28 Jan 2010; published 11 Feb 2010

11. Z. Yuan, Z. Wang, R. Pan, J. Liu, H. Cohen, and Y. Pan, "High-resolution imaging diagnosis and staging of bladder cancer: comparison between optical coherence tomography and high-frequency ultrasound," J. Biomed. Opt. **13**(5), 054007 (2008).
12. Z. G. Wang, D. B. Durand, M. Schoenberg, and Y. T. Pan, "Fluorescence guided optical coherence tomography for the diagnosis of early bladder cancer in a rat model," J. Urol. **174**(6), 2376–2381 (2005).
13. B. Hermes, F. Spöler, A. Naami, J. Bornemann, M. Först, J. Grosse, G. Jakse, and R. Knüchel, "Visualization of the basement membrane zone of the bladder by optical coherence tomography: feasibility of noninvasive evaluation of tumor invasion," Urology **72**(3), 677–681 (2008).
14. F. Koenig, J. Knittel, L. Schnieder, M. George, M. Lein, and D. Schnorr, "Confocal laser scanning microscopy of urinary bladder after intravesical instillation of a fluorescent dye," Urology **62**(1), 158–161 (2003).
15. G. A. Sonn, S. N. Jones, T. V. Tarin, C. B. Du, K. E. Mach, K. C. Jensen, and J. C. Liao, "Optical biopsy of human bladder neoplasia with in vivo confocal laser endomicroscopy," J. Urol. **182**(4), 1299–1305 (2009).
16. M. E. Llewellyn, R. P. J. Barretto, S. L. Delp, and M. J. Schnitzer, "Minimally invasive high-speed imaging of sarcomere contractile dynamics in mice and humans," Nature **454**(7205), 784–788 (2008).
17. B. R. Masters, P. T. C. So, and E. Gratton, "Optical biopsy of in vivo human skin: multi-photon excitation microscopy," Lasers Med. Sci. **13**(3), 196–203 (1998).
18. P. T. C. So, H. Kim, and I. E. Kochevar, "Two-Photon deep tissue ex vivo imaging of mouse dermal and subcutaneous structures," Opt. Express **3**(9), 339–350 (1998).
19. J. C. Malone, A. F. Hood, T. Conley, J. Nürnberger, L. A. Baldridge, J. L. Clendenon, K. W. Dunn, and C. L. Phillips, "Three-dimensional imaging of human skin and mucosa by two-photon laser scanning microscopy," J. Cutan. Pathol. **29**(8), 453–458 (2002).
20. K. König, and I. Riemann, "High-resolution multiphoton tomography of human skin with subcellular spatial resolution and picosecond time resolution," J. Biomed. Opt. **8**(3), 432–439 (2003).
21. K. Steenkeste, S. Lécart, A. Deniset, P. Pernot, P. Eschwège, S. Ferlicot, S. Lévêque-Fort, R. Briandet, and M. P. Fontaine-Aupart, "Ex vivo fluorescence imaging of normal and malignant urothelial cells to enhance early diagnosis," Photochem. Photobiol. **83**(5), 1157–1166 (2007).
22. S. M. Zhuo, J. X. Chen, T. Luo, X. S. Jiang, and S. S. Xie, "Multiphoton microscopy of unstained bladder mucosa based on two-photon excited autofluorescence and second-harmonic generation," Laser Phys. Lett. **6**(1), 80–83 (2009).
23. R. Yadav, S. Mukherjee, M. Hermen, G. Tan, F. R. Maxfield, W. W. Webb, and A. K. Tewari, "Multiphoton microscopy of prostate and periprostatic neural tissue: a promising imaging technique for improving nerve-sparing prostatectomy," J. Endourol. **23**(5), 861–867 (2009).
24. W. Denk, J. H. Strickler, and W. W. Webb, "Two-photon laser scanning fluorescence microscopy," Science **248**(4951), 73–76 (1990).
25. W. R. Zipfel, R. M. Williams, and W. W. Webb, "Nonlinear magic: multiphoton microscopy in the biosciences," Nat. Biotechnol. **21**(11), 1369–1377 (2003).
26. A. Zoumi, A. Yeh, and B. J. Tromberg, "Imaging cells and extracellular matrix in vivo by using second-harmonic generation and two-photon excited fluorescence," Proc. Natl. Acad. Sci. U.S.A. **99**(17), 11014–11019 (2002).
27. W. R. Zipfel, R. M. Williams, R. Christie, A. Y. Nikitin, B. T. Hyman, and W. W. Webb, "Live tissue intrinsic emission microscopy using multiphoton-excited native fluorescence and second harmonic generation," Proc. Natl. Acad. Sci. U.S.A. **100**(12), 7075–7080 (2003).
28. P. J. Campagnola, and L. M. Loew, "Second-harmonic imaging microscopy for visualizing biomolecular arrays in cells, tissues and organisms," Nat. Biotechnol. **21**(11), 1356–1360 (2003).
29. E. Brown, T. McKee, E. diTomaso, A. Pluen, B. Seed, Y. Boucher, and R. K. Jain, "Dynamic imaging of collagen and its modulation in tumors in vivo using second-harmonic generation," Nat. Med. **9**(6), 796–801 (2003).
30. P. P. Provenzano, K. W. Eliceiri, J. M. Campbell, D. R. Inman, J. G. White, and P. J. Keely, "Collagen reorganization at the tumor-stromal interface facilitates local invasion," BMC Med. **4**(1), 38 (2006).
31. R. Cicchi, S. Sestini, V. De Giorgi, D. Massi, T. Lotti, and F. S. Pavone, "Non-linear laser imaging of skin lesions," J. Biophoton. **1**(1), 62–73 (2008).
32. L. H. Laiho, S. Pelet, T. M. Hancewicz, P. D. Kaplan, and P. T. C. So, "Two-photon 3-D mapping of ex vivo human skin endogenous fluorescence species based on fluorescence emission spectra," J. Biomed. Opt. **10**(2), 024016 (2005).
33. P. J. Tadrous, "Methods for imaging the structure and function of living tissues and cells: 2. Fluorescence lifetime imaging," J. Pathol. **191**(3), 229–234 (2000).
34. P. J. Tadrous, J. Siegel, P. M. W. French, S. Shousha, N. Lalani, and G. W. H. Stamp, "Fluorescence lifetime imaging of unstained tissues: early results in human breast cancer," J. Pathol. **199**(3), 309–317 (2003).
35. Y. Chen, and A. Periasamy, "Characterization of two-photon excitation fluorescence lifetime imaging microscopy for protein localization," Microsc. Res. Tech. **63**(1), 72–80 (2004).
36. S. Y. Breusegem, M. Levi, and N. P. Barry, "Fluorescence correlation spectroscopy and fluorescence lifetime imaging microscopy," Nephron, Exp. Nephrol. **103**(2), e41–e49 (2006).
37. R. Cicchi, D. Massi, S. Sestini, P. Carli, V. De Giorgi, T. Lotti, and F. S. Pavone, "Multidimensional non-linear laser imaging of Basal Cell Carcinoma," Opt. Express **15**(16), 10135–10148 (2007).
38. R. Cicchi, L. Sacconi, A. Jasaitis, R. P. O'Connor, D. Massi, S. Sestini, V. De Giorgi, T. Lotti, and F. S. Pavone, "Multidimensional custom-made non-linear microscope: from ex-vivo to in-vivo imaging," Appl. Phys. B **92**(3), 359–365 (2008).

#119986 - $15.00 USD Received 18 Nov 2009; revised 26 Jan 2010; accepted 28 Jan 2010; published 11 Feb 2010

39. S. J. Lin, R. J. Wu, H. Y. Tan, W. Lo, W. C. Lin, T. H. Young, C. J. Hsu, J. S. Chen, S. H. Jee, and C. Y. Dong, "Evaluating cutaneous photoaging by use of multiphoton fluorescence and second-harmonic generation microscopy," Opt. Lett. **30**(17), 2275–2277 (2005).
40. J. Paoli, M. Smedh, A. M. Wennberg, and M. B. Ericson, "Multiphoton laser scanning microscopy on non-melanoma skin cancer: morphologic features for future non-invasive diagnostics," J. Invest. Dermatol. **128**(5), 1248–1255 (2008).
41. O. Warburg, "The metabolism of tumors," Constabel, London (1930).
42. M. C. Skala, K. M. Riching, D. K. Bird, A. Gendron-Fitzpatrick, J. Eickhoff, K. W. Eliceiri, P. J. Keely, and N. Ramanujam, "*In vivo* multiphoton fluorescence lifetime imaging of protein-bound and free nicotinamide adenine dinucleotide in normal and precancerous epithelia," J. Biomed. Opt. **12**(2), 024014 (2007).
43. D. K. Bird, L. Yan, K. M. Vrotsos, K. W. Eliceiri, E. M. Vaughan, P. J. Keely, J. G. White, and N. Ramanujam, "Metabolic mapping of MCF10A human breast cells via multiphoton fluorescence lifetime imaging of the coenzyme NADH," Cancer Res. **65**(19), 8766–8773 (2005).
44. M. C. Skala, K. M. Riching, A. Gendron-Fitzpatrick, J. Eickhoff, K. W. Eliceiri, J. G. White, and N. Ramanujam, "*In vivo* multiphoton microscopy of NADH and FAD redox states, fluorescence lifetimes, and cellular morphology in precancerous epithelia," Proc. Natl. Acad. Sci. U.S.A. **104**(49), 19494–19499 (2007).

1. Introduction

Bladder cancer is the fifth most common cancer in U.S [1]. In general, it is curable when detected and treated early. A more accurate early diagnosis of bladder cancer would be a suitable aim for both detection and treatment. Diagnostic methods used are different, even if a non-invasive early detection of bladder cancer is still a challenge. Very often, symptomatic patients are visually inspected through white light cystoscopy, which is the most diffused endoscopic technique for bladder cancer detection in the clinical routine. This simple and easy-to-use technique is able to visualize the urothelium surface. The diagnosis is demanded to the eye of an experienced MD. However, cystoscopy is not able to assess bladder cancer in early stage but just lesions in a developed stage.

Sensitivity and specificity of cystoscopy can be significantly improved by means of fluorescence coming from photosensitizers used as contrast agents [2–5]. Various compounds as such methyl-aminolevulinate can be used to enhance cancer margins contrast. This technique has the big advantage of being performed with the same cystoscope used for common inspection (under UV or blue-illuminaton) as well as of providing better sensitivity (up to 96%) with respect to white light cystoscopy (up to 77%). Nevertheless its specificity is still far from being optimal (up to 60-70%), resulting in a high percentage of false positives. Specificity can be improved by means of tissue autofluorescence spectroscopy [6,7] which is mainly performed by means of a fiber-probe inserted in the service channel of a cystoscope. Such a technique can be used combined with white light cystoscopy [8], or also with photosensitizers and fluorescence cystoscopy [9,10]. Fluorescence emission spectrum measurement gives additional information helpful in discriminating pathologic conditions. Further, coupled with cystoscopy, this technique allows to target only visually ambiguous lesions, helping in diagnosing when clinical eye fails.

Recently, new non-invasive techniques, using both optical and non-optical methods, have been used for bladder cancer detection. Among them, high-frequency ultra-sound (HFUS) is able to image inside a tissue up to 5-10 mm depth but with poor spatial resolution compared to optical methods. Optical coherence tomography (OCT) is giving an optical alternative to HFUS, by enabling non-invasive and high-resolution biomedical imaging modality [11]. OCT has found potential applications for the diagnosis of diseases in various biological tissues, including bladder cancer [12,13]. For other modern imaging techniques, such as laser-scanning imaging techniques, there is currently a big challenge to setup them in modern endoscopes. New technologies for scanning systems miniaturization (MEMS, ultra-sound scanning devices), for pulse delivery optimization (PCF, hollow-core fibers) as well as for miniaturization of high-NA optics (GRIN-lenses) have created new insights for both single- and multi-photon endoscopic imaging. In the last years several developments were done in the field of confocal endoscopy, giving rise to a growing number of research instruments and also to few commercial flexible endoscopes. Both confocal microscopy [14] and endoscopy [15] have already been used for imaging *ex-vivo* samples of human bladder. Even if non-linear flexible endoscopic imaging is still a challenge, SHG endoscopic imaging has already been

#119986 - $15.00 USD Received 18 Nov 2009; revised 26 Jan 2010; accepted 28 Jan 2010; published 11 Feb 2010

performed *in-vivo* by means of a rigid needle with a GRIN-lens optically coupled to the microscope objective [16]. According to the capabilities that non-linear imaging techniques have already largely shown in providing "optical biopsy" of a tissue [17–20], in the next future non-linear endoscopy would represent a breakthrough in the urology field for both early diagnosis and therapy follow-up of bladder cancer. In two recent studies, the authors have used non-linear imaging microscopy on bladder cell cultures [21] as well as on bladder tissue samples from animals [22,23]. Nevertheless, a test on the capabilities of multi-photon microscopy in detecting human bladder cancer have not been reported so far. In this paper, we firstly describe the application of two-photon microscopy to human bladder tissue imaging and characterization.

Among non-linear imaging techniques used, two-photon excitation fluorescence (TPEF) microscopy [24] is providing high-resolution deep tissue imaging [17–20]. Since both cells and extracellular matrix intrinsically contain several fluorescent molecules with absorption in the UV range (NADH, tryptophan, keratins, melanin, elastin, cholecalciferol and others), biological tissues can be imaged by TPEF microscopy without any exogenously added probe [25–27]. Second-harmonic generation (SHG) is a well suited microscopy technique to analyze connective tissues due to the significant second order non-linear susceptibility of collagen [28,29]. SHG signal has been used to discriminate cancerous tissue [29] as well as collagen modifications in the peri-tumoral stroma [30,31]. Multispectral two-photon (MTPE) imaging, performed by detecting the emission spectrum of endogenous fluorescence, offers functional information about the relative quantities of fluorescent molecules, which correlate with tissue structure in physiological and pathological states [32]. Fluorescence lifetime imaging microscopy (FLIM) is an additional non-invasive microscopy technique enabling the identification of endogenous fluorescence species by measuring the decay rate of their fluorescent emission [33,34]. FLIM is useful to study protein localization [35] and fluorescent molecular environment [36].

In this work we used a multidimensional analysis [37] for bladder tissue characterization by combining all the non-linear microscopy techniques described above. In particular, we performed a morphological analysis of bladder urothelium by using TPEF and SHG on fresh biopsies. Compared to healthy mucosa (HM), carcinoma in situ (CIS) showed differences in morphology, measured in terms of cellular-to-nuclear dimension ratio. MTPE analysis of fluorescence signals showed similar emission spectra but with a different SHG contribution. Deeper analysis and discrimination was performed by measuring the SHG-to-autofluorescence signal ratio through a normalized index. Further characterization was obtained by the use of spectral- and time-resolved detection of endogenous NADH and FAD fluorescence. First, by selecting spectral channels corresponding to NADH and FAD emission, a different fluorescent intensity ratio was found between HM and CIS. Then, by a double-component lifetime analysis of FLIM images, differences in the lifetime components ratio between the two tissues were highlighted. Even if a more significant statistics on a large number of samples, including mild- and low-grade bladder cancers, would be helpful to give more indication on the diagnostic sensitivity and specificity of the method, this multidimensional analysis may represent a powerful tool, if combined with multi-photon endoscopy, with confocal endoscopy or with fluorescence fiber-based spectroscopy, for the early diagnosis of bladder cancer.

2. Materials and methods

2.1 Samples

Two sets of cold-cup bladder biopsies of healthy mucosa and white light cystoscopy pattern suspected of CIS were taken in 5 patients with positive urine cytology during transurethral resection of the bladder. One set of the specimens were sent for pathology and the other stored in a wet environment with few drops of normal saline and sent for two-photon imaging within 1 hour. Pathology report confirmed CIS in all the samples.

#119986 - $15.00 USD Received 18 Nov 2009; revised 26 Jan 2010; accepted 28 Jan 2010; published 11 Feb 2010

Fresh relaxed biopsies were sandwiched between a microscope slide and a 170 μm glass coverslip. A fat silicon ring was used to both create a chamber for the sample and to prevent unwanted movements of the coverslip. Some droplets of PBS were added to the sample to maintain natural osmolarity. Samples were imaged with two-photon microscopy within one hour from excision, always using "en-face" optical sectioning geometry.

2.2 Non-linear microscopy system

The experimental setup consisted of a custom-made upright non-linear microscope able to perform combined TPEF-SHG by detecting emitted photons in proportional regime, and FLIM-MTPE by working in single-photon counting regime. Detailed description of this microscope, including acquisition and control, are given in [38].

2.3 Image acquisition and analysis

2.3.1 Morphological analysis (TPEF and SHG)

The excitation was done by using a wavelength of 740 nm for TPEF and 840 nm for SHG, and a mean laser power at the sample between 10 and 40 mW, depending on the depth of recording. TPEF and SHG images were acquired with 1024 × 1024 pixels spatial resolution, from 100 μm to 200 μm field of view dimension, using a pixel dwell time of 5 μs. Image processing was performed by using ImageJ (NIH, Bethesda, Maryland, US). Acquired 8-bit TPEF and SHG images were merged in RGB images (color-code: green for TPEF and blue for SHG) to be presented together with histological images. Further processing was done on TPEF images. A threshold was applied to images of cells to remove background, enhancing both cellular and nuclear borders. Then the borders were visually selected and the inner area measured in $pixel^2$ units. Finally the cellular-to-nuclear area ratio was calculated. This analysis was performed on approximately 10 cells per sample, on images taken at a depth in the 20-30 μm range.

2.3.2 Spectral-resolved analysis (MTPE)

Two excitation wavelengths were used: 740 nm for exciting NADH, and 890 nm for FAD, and a mean laser power of approximately 15 mW. MTPE images were acquired in blocks of 16 spectral images (420 nm - 620 nm spectral range) with 32 × 32 pixels spatial resolution, 20 μm field of view dimension, using a pixel dwell time of 0.2 ms and an integration time of approximately 160 s per image block. Acquired files were exported in three-dimensional matrixes representing the number of detected photons $N=N(x,y,\lambda)$ as a function of position and wavelength by using SPC-Image 2.8 (Becker-Hickl GmbH, Berlin, Germany) and processed by using a custom routine developed under LabView 7.1 (National Instruments, Austin, TX, US). Two normalized ratio-based methods were used for spectral analysis of images acquired at the two depths of 20 μm to 30 μm, and of 50 μm to 60 μm, respectively corresponding to mid-urothelium and to urothelium-lamina propria border in HM. Measurements were performed at corresponding depths in both HM and CIS samples. For deeper images the following normalized ratio, known as SHG-to-autofluorescence ageing index of dermis [39] (SAAID), was used as a score:

$$SAAID = \frac{SHG - TPEF}{SHG + TPEF}. \quad (1)$$

In SAAID scoring at 890 nm excitation wavelength, SHG image is the sum of all channels in the 420 nm – 460 nm spectral range, whereas TPEF is the sum of all channels in the 475 nm – 620 nm spectral range. Images taken at a depth of 20-30 μm were used for Red-Ox ratio scoring. In this analysis NADH-image is intended as the image acquired on a single channel (460 nm – 473 nm) at 740 nm excitation wavelength, whereas FAD-image is intended as the image acquired on a single channel (508 nm – 521 nm) at 890 nm excitation wavelength. Numbers of detected photons were corrected for detector spectral response and to the square

#119986 - $15.00 USD Received 18 Nov 2009; revised 26 Jan 2010; accepted 28 Jan 2010; published 11 Feb 2010

of the excitation power measured at the objective aperture. Red-Ox ratio was calculated by using the following relationship:

$$ROx = \frac{FAD - NADH}{FAD + NADH}. \quad (2)$$

Both SAAID and ROx scoring results are presented in color-coded maps as well as histogram distribution of the raw calculated values, together with the corresponding look-up table of the map superimposed.

2.3.3 Time-resolved analysis (FLIM)

Two excitation wavelengths were used and two corresponding spectral bands for detection: 740 nm for exciting NADH (430 nm - 490 nm detection) and 890 nm for FAD (470 nm – 550 nm detection). FLIM images were acquired with a mean laser power of approximately 15 mW, 128 × 128 pixels spatial resolution, 100 μm field of view dimension, using a pixel dwell time of 0.2 ms, an integration time of approximately 40 s per image and a temporal binning of 256 bins over a 12.5 ns TAC range. System response de-convolution and fluorescence decay fits on image pixels were done by using a double-exponential decay model in SPC-Image 2.8 (Becker-Hickl GmbH, Berlin, Germany), which also allows to present data as a fit parameter map. Graphs and histograms were prepared by using Microcal Origin Pro 8.0 (OriginLab Corporation, Northampton, MA, US).

3. Results and discussion

3.1 Tissue morphology (TPEF-SHG)

Morphological features of bladder urothelium can be highlighted on fresh biopsies by taking advantage of NADH autofluorescence, which is still present inside a fresh biopsy after excision [27,32]. Both HM bladder cells and CIS cells give a high fluorescent signal if imaged within 2-3 hours from excision (see Fig. 1). In these measurements we used an excitation wavelength of 740 nm for TPEF and of 840 nm for SHG, which are adequate to excite NADH fluorescence and collagen SHG, respectively. Both TPEF and SHG allow sub-diffraction limit spatial resolution, enabling bladder urothelium imaging at the sub-cellular level. A good agreement was found between TPEF-SHG images and the corresponding histological images taken after histological examination of the same samples (Fig. 1).

The more interesting result arisen from morphological analysis is related to the different cellular-to-nucelar dimension ratio between HM cells and CIS cells. From the acquired images, a larger nuclear dimension of CIS cells is clearly distinguishable. To give a more quantitative measurement, 10 cells per sample were selected on images taken at a depth range of 20-30 μm in both HM and CIS, and their cellular and nuclear membrane borders were highlighted by thresholding and background removing. Then, the dimension of both whole cells and nuclei were measured and their ratio calculated. The obtained results are plotted in a bar histogram in Fig. 2, showing a smaller ratio for CIS with respect to HM. The limited number of cells chosen for the analysis is due to the needing of imaging samples as fresh as possible as well as to the long time required for both FLIM and MTPE acquisition. Even if this morphological signature of tumor cells has already been measured by TPEF microscopy in other tissues, such as skin [40], further analysis on a larger data set would be helpful to confirm this promising result.

#119986 - $15.00 USD Received 18 Nov 2009; revised 26 Jan 2010; accepted 28 Jan 2010; published 11 Feb 2010

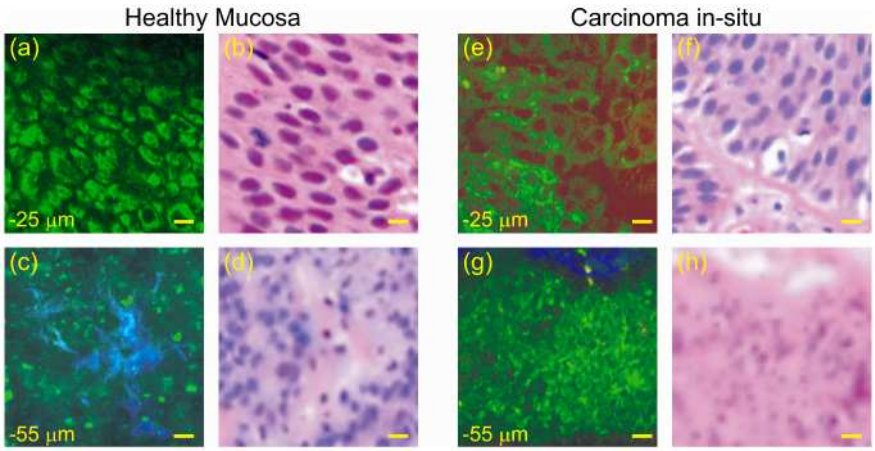

Fig. 1. Combined TPEF (green-coded) and SHG (blue-coded) images taken from human ex-vivo fresh biopsies of bladder and the corresponding histological images taken after H&E staining of the same sample. On the left: an optical section of healthy mucosa acquired at 25 μm depth (a), and the corresponding histological image (b); an optical section of HM / connective tissue border acquired at 55 μm depth (c) and the corresponding histological image (d). On the right: an optical section of CIS acquired at 25 μm depth (e), and the corresponding histological image (f); an optical section of CIS / connective tissue border acquired at 55 μm depth (g) and the corresponding histological image (h). Scale bars: 10 μm.

An additional morphological feature noted by researchers during measurement sessions is in average a higher SHG signal coming from HM with respect to CIS. This finding was confirmed by MTPE measurements, described below.

3.2 Tissue spectral features (MTPE - SAAID and ROx scoring)

In a first set of measurements MTPE analysis was performed by using 740 nm and 890 nm excitation wavelength and 16 detection channels in the 420 nm – 620 nm range. The spectra shown in Figs. 3(a) and 3(b) are the average of the acquired spectra. Each data point represents the sum of detected photons in a 20 μm by 20 μm laser-scanned region-of-interest, taken in a depth range of 50-60 μm from tissue surface, averaged on 5 samples for both HM and CIS. As it can be noted in Fig. 3(a) and 3(b), the fluorescence emission spectra are quite similar for the two tissues. In particular, the two spectra are coinciding on the whole detection range at 740 nm excitation (Fig. 3(a)) but only on the longer wavelengths at 890 nm excitation (Fig. 3(b)), where they exhibit a difference around 440 nm. This effect is due to SHG contribution, which is detectable in our detection range only at 890 nm excitation (445 nm emission). A lifetime analysis (data not shown) on the channels in the 420 nm – 460 nm range has confirmed the hypothesis of a SHG signal. This effect is probably due to a higher cellular proliferation in CIS with respect to HM, resulting in a statistically lower probability to get SHG signal coming from the underlying connective tissue. A scoring method based on the SAAID index (normally used for scoring skin photo-ageing [39]) helped in quantifying this

#119986 - $15.00 USD Received 18 Nov 2009; revised 26 Jan 2010; accepted 28 Jan 2010; published 11 Feb 2010

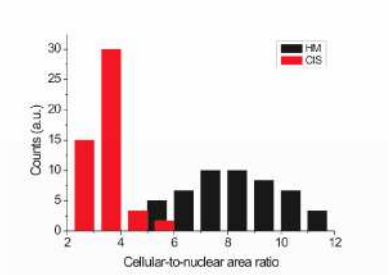

Fig. 2. Histogram distribution of the cellular-to-nuclear area ratio (d) for CIS (in red) and for HM (in black), calculated by summing over images acquired in a 20-30 μm, on 5 samples of CIS and 5 samples of HM and over 10 cells per sample.

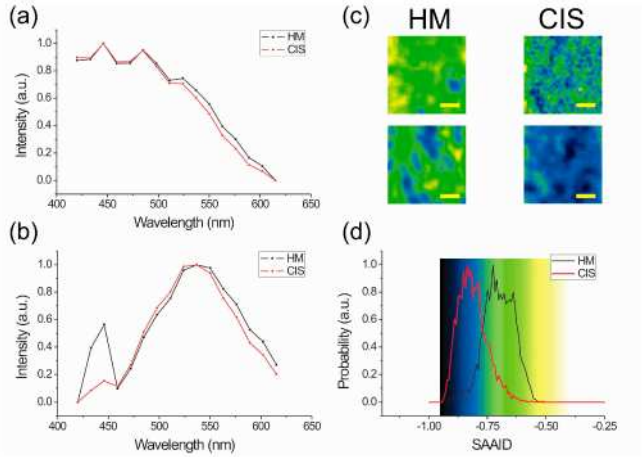

Fig. 3. Two-photon emission spectra for CIS (red) and for HM (black), measured by summing the detected photon number over a region of 20 μm × 20 μm at a depth of 50-60 μm, and by averaging on 5 samples of CIS and 5 samples of HM, for 740 nm excitation (a), and for 890 nm excitation (b). Two examples of SAAID maps (c), calculated using Eq. (1), for both CIS and HM presented in a color-coded scale. Scale bars: 5 μm. SAAID distribution for CIS (red) and for HM (black) with the color-coded scale used in SAAID mapping superimposed (d), obtained by summing the calculated SAAID index over a region of 20 μm × 20 μm, and after averaging on 5 samples of CIS and 5 samples of HM.

effect. Two examples of SAAID maps are shown for both HM and CIS (Fig. 3(c)). The poor spatial resolution of these maps is due to the fact that in the system used, the increasing of spectral and temporal channels has to be paid in terms of a reduction of scanned pixels. The graph represented in Fig. 3(d) is the normalized distribution of the SAAID index, averaged on 5 samples for both HM and CS. Higher SHG contribution should correspond to a higher value of SAAID index, as it has been observed for HM and confirmed by data analysis. Even if this datum is not representing a strong feature for tissue discrimination, SHG microscopy is confirmed to be helpful in tissue assessment. Moreover, it represents a promising tool to enlarge the study to other cancer features such as the relationship between cancer growth and collagen disruption.

In a second set of measurement MTPE was performed with particular attention to the excitation of NADH and FAD by using two excitation wavelengths and two corresponding single-channel for detection, as follows: NADH (740 excitation; 459 – 472 nm detection), FAD (890 nm excitation; 511 – 524 nm detection). Acquired images (in Figs. 4(a) and 4(b) there is an example of acquisition in HM at 740 nm and 890 nm, respectively) were processed and, by using the relationship defined in Eq. (2), the ROx index was calculated and presented as a ROx map in a color-coded scale (see Fig. 4(c) for both HS and CIS). As above, the poor

#119986 - $15.00 USD Received 18 Nov 2009; revised 26 Jan 2010; accepted 28 Jan 2010; published 11 Feb 2010

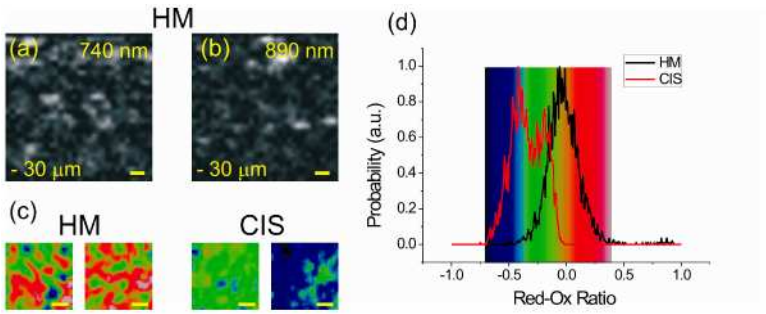

Fig. 4. MTPE images of HM acquired: at 740 nm excitation wavelength and detected in the 459 nm – 472 nm spectral range (a); at 890 nm excitation wavelength and detected in the 511 nm – 524 nm spectral range (b). Scale bars: 2 μm. Two examples of ROx maps (c), calculated using Eq. (2), for both CIS and HM presented in a color-coded scale. Scale bars: 5 μm. Red-Ox ratio distribution for CIS (red) and for HM (black) with the color-coded scale used in ROx mapping superimposed (d), obtained by summing the calculated ROx index over a region of 20 μm × 20 μm, and after averaging on 5 samples of CIS and 5 samples of HM.

spatial resolution of these maps is related to the system used. The graph in Fig. 4(d) is showing the ROx distribution of HM and CIS, averaged on 5 samples each. A higher value of HM in comparison to CIS is confirming a lower oxidative stress in normal tissue with respectto cancer. In fact, according to the Warburg effect [41], cancer cells produce more energy by glycolysis biochemical pathway in comparison to healthy cells in which phosphorilation dominates. The consequence is an unbalance in the amount of NADH/FAD couple as well asin their oxidative states. This effect can be optically detected by inducing fluorescence of the NADH/FAD couple and by measuring fluorescence intensity ratio for Red-Ox ratio, or by measuring fluorescence lifetime for discriminating oxidative and reduced state of the two molecules. Such a technique was recently used to optically detect Red-Ox state of cells and tissues in healthy, dysplastic or neoplastic condition [42]. Further analysis can be performed by measuring fluorescence lifetime of both NADH and FAD, as described below.

3.3 Fluorescence lifetime of NADH-FAD couple (FLIM)

Lifetime analysis was performed by using 740 nm and 890 nm excitation wavelength. Two fluorescence filters centered at 460 nm and 510 nm allowed to selectively detect NADH and FAD fluorescence, respectively. Fluorescence decay traces fits were performed after system response de-convolution by using a double-exponential decay function in order to take into account both free and protein-bound state of the two molecules. Similar analysis has already been performed on both cell cultures [43], and also on fresh punch biopsies from animals [44], resulting in a difference in the ratio of free/protein-bound NADH and FAD between healthy and precancerous tissue, as well as in a variation in both fast and slow lifetime components. In the double-exponential decay model the fast component is related to free-NADH and the slow component to protein-bound NADH, and vice-versa for FAD. The three fit parameters are: the two lifetime components (fast and slow) and their coefficient ratio. In particular, the ratio of the components is representing the ratio free/protein-bound for NADH, and the ratio protein-bound/free for FAD. In this paper the analysis is limited to the study of the ratio of the two components, whereas the lifetime analysis on separated components has not been performed. In Fig. 5 the results are presented in a panel where a image representing a lifetime components ratio in a color-coded scale is shown for both HM (Fig. 5(a,b)) and CIS (Fig. 5(c,d)). The two graphs are representing the distributions of the lifetime components ratio of both HM and CIS, calculated for excitation of NADH at 740 nm (Fig. 5(e)) and of FAD at 890 nm (Fig. 5(f)), averaged on 5 samples per tissue type. Theobtained results are in agreement with what has been already found for precancerous and cancerous tissues in both cell culture and animal model: a higher relative concentration of protein-bound NADH and of free FAD is characterizing CIS in comparison to HM, where the

#119986 - $15.00 USD Received 18 Nov 2009; revised 26 Jan 2010; accepted 28 Jan 2010; published 11 Feb 2010

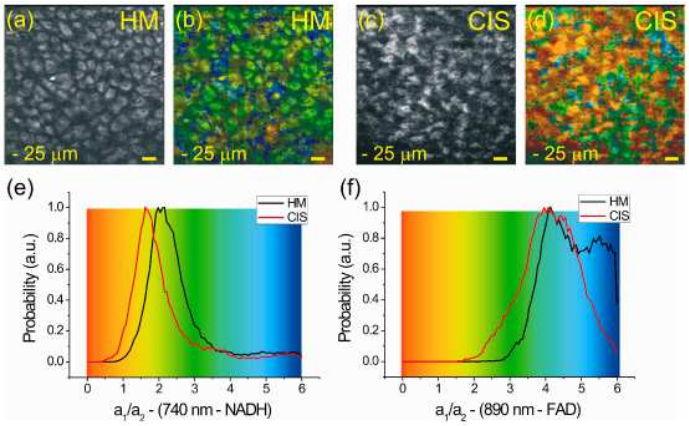

Fig. 5. TPEF image (a) and corresponding lifetime ratio map (b) acquired in HM sample at 25 µm. TPEF image (c) and corresponding lifetime ratio map (d) acquired in CIS at 25 µm depth. Scale bars: 10 µm. Excitation wavelength: 740 nm. Detection band: 430-490 nm. Lifetime components ratio distribution for CIS (red) and for HM (black) at 740 nm (e) and 890 nm (f) excitation wavelength, obtained by summing the parameter over a cellular region of 128 µm × 128 µm at a depth in the 20-30 µm range, and averaging on 5 samples of CIS and 5 samples of HM.

opposite shift has been found. This result is someway related to the result found in the previous section by Red-Ox ratio measurement. In fact the relative amount of free-bound NADH and FAD should be related with the cellular metabolic state of a tissue [44]. An observation on tissue degradation should be done at this point, especially if considering Red-Ox and lifetime measurements. Even if in a tissue biopsy degradation, including oxidation, should start immediately after excision, NADH and FAD can be used to image a fresh biopsy [27,32]. Certainly, the time between excision and imaging can affect the measured values, especially for *ex-vivo* samples. Anyway, in a time-lapse measurement performed on two samples (data not shown), a negligible variation of fluorescence lifetime has been observed for both HM and CIS over 2 hours. The measurement started approximately one hour after excision. Even if some slightly different values are expected from *in-vivo* measurements, the method presented here can be considered a promising tool to optically record the Red-Ox state of a tissue and its application in *in-vivo* imaging could be useful in early diagnosis of cancerous and precancerous tissues, as well as in the follow-up of cancer-targeted therapies.

4. Conclusions

In conclusion, in this work we demonstrated the capability of our multidimensional method to discriminate between HM and CIS on *ex-vivo* fresh biopsies of bladder. Both morphological and spectroscopic differences were found between the two tissue types. In particular, differences were found in the cellular-to-nuclear area ratio, in the SHG-to-autofluorescence ratio (measured by SAAID scoring), in the Red-Ox ratio as well as in the fluorescence lifetime components ratio of both NADH and FAD. Further analysis, as well as a more significant statistics on a larger number of samples, would be suitable to confirm our encouraging results. Next steps of this work, beyond the aim of this paper, are: the confirmation of the already obtained results through the analysis of a larger number of samples; the extension of the analysis to other bladder lesions to assess the capabilities of the method in discriminating cancer in low- and mild-grade. Once measured its diagnostic capability on a wide range of bladder lesions, the presented method could become a promising tool to be used in a multiphoton endoscope or in a spectroscopic probe with the final goal of improving white light cystoscopy diagnostic accuracy. Moreover, similar analytical methods may be applied to study several pathologic diseases of biological tissues. On account of the emerging potential of non-linear imaging to become an *in-vivo* diagnostic tool, the proposed methods may find future application in the clinical setting.

#119986 - $15.00 USD Received 18 Nov 2009; revised 26 Jan 2010; accepted 28 Jan 2010; published 11 Feb 2010